A 3D Progressive Failure Model for predicting pseudo-ductility in hybrid unidirectional composite materials under fibre tensile loading

J.M. Guerrero[a,*], J.A. Mayugo[a], J. Costa[a], A. Turon[a]

[a]*AMADE, Polytechnic School, Universitat de Girona, Campus Montilivi s/n, E-17003 Girona, Spain*

Abstract

This paper presents a three-dimensional Progressive Failure Model based on the chain of bundles able to represent the stiffness loss in unidirectional composite materials loaded in the fibre direction. A representative volume element with a random distribution of fibres with their own radius is considered. Complete stress distributions around fibre breaks are obtained by associating a damage variable to the loss of stress transfer capability along the ineffective length and applying local stress concentrations. The model has been validated by comparing it against the literature results and exhibits good agreement with hybrids and non-hybrid composites. The aim of this model is to simulate the tensile response of unidirectional composite systems dominated by fibre fragmentation mechanisms using a very reduced computational effort, even for larger representative volume elements, compared to micro-mechanical finite element models.

Keywords: A. Hybrid, A. Polymer-matrix composites (PMCs), C. Computational modelling, C. Micro-mechanics

1. Introduction

Fibre reinforced polymers (FRP) are widely used in lightweight structures mainly thanks to their high specific strength and stiffness. However, their quasi-brittle behaviour and low toughness leads to fibre tensile failure with hardly any prior damage symptoms, thus limiting their use and applicability [1]. One potential way to solve this problem is with fibre hybridization [2]. In a hybrid composite, two kinds of fibres with different

---

*Corresponding author. Tel.: +34 972 41 88 17.
Email address: `josemanuel.guerrero@udg.edu` (J.M. Guerrero)

longitudinal failure strains are mixed. The mixture can be arranged on three different scales [2], which are also able to be combined into: i) interlayer or layer-by-layer i.e. by mixing layers of different fibres, ii) intralayer or yarn-by-yarn i.e. by mixing the fibres within the layers but not within the separate yarns, and iii) intrayarn or fibre-by-fibre i.e. by mixing the fibres completely at the yarn/tow.

A low elongation fibre (LE) has a low failure strain and a high elongation fibre (HE) has a high failure strain. Thanks to this combination, the LE failure strain in a hybrid can be larger than that in a non-hybrid composite. This phenomenon is known as the hybrid effect [3]. Moreover, with the appropriate hybridization design, a progressive failure of fibres under tensile load can be induced leading to pseudo-ductile behaviour [4]. Currently [2], to explain the hybrid effect the scientific community outlines three main reasons: i) changes in the development of the failure, ii) thermal residual stresses and iii) dynamic effects.

Nowadays, changes in the failure propagation are assumed to be the main reason for the hybrid effect. Because of the presence of flaws, the strength of brittle fibres is not deterministic and follows a statistical distribution. When a fibre breaks, shear stresses are transferred from the fibre to the matrix. As a consequence, the broken fibre recovers its stress in a distance called the ineffective length, whereas the surrounding fibres withstand stress concentration. Eventually, the neighbouring fibres of each broken fibre fail, thus initiating several clusters of broken fibres which grow further upon loading. When one of these clusters reaches a certain size, it propagates unstably and leads to the final failure. Other phenomena, such as debonding, matrix cracking or yielding and fibre pullout, may also contribute. Notwithstanding, in a hybrid composite the differences between the elastic and geometrical properties and the failure strains can alter and delay the formation of clusters. Moreover, by reducing the quantity of LE fibres in the hybrid, LE failure strain can also be increased because of the size effects [5].

An additional and secondary cause of the hybrid effect is related to the residual stresses generated during the manufacturing process [2]. Residual stresses appear when mixing different populations of fibres with dissimilar thermal expansion coefficients, which leads to different residual stresses in each fibre population.

The third reason given for the hybrid effect is the dynamic effect in the process of

tensile failure. When a fibre breaks, the elastic energy that was sustained by that fibre is released and becomes kinetic energy which dampens after some time. During this period, dynamic loads propagate through the composite and increase the probability of failure. However, in the case of a hybrid composite, the dynamic phenomena can be altered. Xing *et al.* [6] demonstrated that in a hybrid composite two out-of-phase stress waves, one for each fibre population, propagate after an LE fibre break. If both waves compensate each other, lower dynamic loads are produced, leading to larger failure strains. However, this topic has not been studied in depth and its importance remains unclear [2, 7].

In addition, the hybrid effect is also influenced somewhat by different parameters which include the relative volume fraction between both fibres, strength distribution, fibre dispersion, fibre stiffness ratios and the failure strain ratio. Other parameters, such as the matrix stiffness or debonding, have no clear influence [3]. Moreover, the specimen size effect on the hybrid effect is also unknown [8].

Over the past decades different authors have attempted to study hybrid composites under fibre tensile loading. Hayashi [9] was the first author who observed the hybrid effect in a carbon-glass layer-by-layer hybrid in an experimental test. Later, Zweben [10] extended a shear-lag model to hybrid composites to obtain the hybrid effect analytically. While Fukuda [11] improved the model further, it still has major limitations. According to Swolfs *et al.* [3], Fukuda's and Zweben's models can be used as the upper and lower bounds for predicting the hybrid effect.

Recently, Tavares *et al.* [12] presented a fibre-by-fibre micro-mechanical finite element model (FEM) simulating fibre, matrix and fibre-matrix interphase damage [13]. The results demonstrated the importance of the failure strain ratio of both fibres, the statistical strength distribution and a progressive failure between both HE and LE fibres in obtaining pseudo-ductility. However, the model requires high computational resources and is limited to simulating a small number of fibres.

Okabe *et al.* [14, 15] presented an advanced shear-lag model able to represent the fibre failure process of composite materials. The model represents the fibres through tensile springs and the matrix through shear springs. The advantage of these types of models is that they are simpler, faster and cheaper in computational cost than FEM models are. Furthermore, they are still able to simulate the key physics involved, without being limited

to only a few fibres as in the FEM approach. However, Okabe *et al.*'s model is limited to hexagonal or square packings, which do not allow hybrid composites with fibres of different radii to be studied.

Swolfs *et al.* [3, 5, 16–18] presented a strength model under the assumption of a local load sharing rule, based on the chain of bundles approach from Rosen [19], Okabe *et al.* [14, 15] and others [20, 21]. Unlike the model of Okabe *et al.*, a random fibre packing with each fibre with its own radius was considered. With their model, Swolfs *et al.* demonstrated that larger LE strength dispersions, lower number of LE fibres, higher HE fibre stiffness or larger failure strain ratios all ultimately lead to greater hybrid effects. Fibre dispersion also showed an evident impact. However, Swolfs' model [3, 5, 16–18] attempts to predict the behaviour only up to the onset of LE fibre fragmentation, because it does not capture a non-linear response attributable to fragmentation mechanisms. Thus, it is unable to predict pseudo-ductility.

In recent years, an increase in the amount of experimental work conducted concerning fibre hybridization has also been seen. Czél and Wisnom [22] hybridized thin carbon fibre prepreg plies with standard thick plies of glass fibres. They found pseudo-ductility with specimens of one and two plies of thin carbon. However, specimens with three and four plies failed with unstable delamination. Later, Wisnom *et al.* [8] obtained similar findings. Moreover, they compared their results with a simplified version of Swolfs *et al.* [5] strength model and obtained good agreement. Yu *et al.* [23] also manufactured intermingled hybrid composites using aligned discontinuous fibres. By combining high-modulus carbon and E-glass in the hybrid, good pseudo-ductile responses were also obtained as a result of the carbon fibres fragmentation. Further to this, Jalalvand *et al.* [24] developed a new simple analytical method to predict all possible damage mode maps in unidirectional hybrid composites. By using the method as a design guideline, new hybrid specimens of a standard-thickness glass/thin-ply carbon hybrid were manufactured and tested, leading to a good pseudo-ductile response. Quite recently, Fotouhi *et al.* [25] tested quasi-isotropic high performance thin-ply carbon/glass hybrid laminates. Pseudo-ductility was also obtained in all fibre orientations under tensile loading. Last but no least, Czél *et al.* [26] hybridized thin-ply unidirectional interlayer all carbon-epoxy composites comprising high modulus and high strength. Again, large pseudo-ductile responses were

obtained.

Despite advances in the modelling and understanding of hybrid composites, there is no local load sharing model for these materials that is capable of representing the pseudo-ductile behaviour within a random distribution of fibres. At the moment, the exception to this are the micro-mechanics FEM models which require huge computational resources and so are unsuitable as a design tool or to perform parametric studies.

In the present work, the authors propose a new three-dimensional Progressive Failure Model, (called here PFM) based on the chain of bundles which is able to accurately represent both progressive damage and pseudo-ductile behaviour in unidirectional composites. The proposed model implicitly allows fibre fragmentation mechanisms to be captured, thus estimating multiple breaks along the length of the fibre. A random distribution of fibres of a given radius is considered. The methodology leads to different deformations along the model, using the hypothesis that fibres work in parallel but taking into account the local stress fields around each fibre break. The complete stress distribution around the fibre breaks is obtained through two dependent approaches. Firstly, a damage variable related to fibre breaks and to a shear-lag model is computed. Secondly, local stress concentrations are applied through all stress recoveries. Thermal residual stresses and dynamic loads are omitted but the model framework allows for its future implementation. The remainder of this paper is as follows: firstly, we present the model, which we then validate by comparing it with the literature results, and finally some conclusions are drawn.

2. Chain of bundles progressive failure model

2.1. Definition of the fibre random distributed RVE

A representative volume element (RVE) with a random distribution of fibres is generated to capture the interaction between the fibres and the matrix. The RVE represents, on a micro-mechanical scale, a portion of a real material model containing the matrix and a sufficient number of fibres. According to Trias *et al.* [27] and Zangernberg *et al.* [28], the minimum transversal size of the RVE in an elastic model should be 50 times the fibre radius ($50 \times R$). However, in a model with damage, the minimum size of the RVE could be even larger to capture the fibre effects. Similarly, the RVE length in the fibre

longitudinal direction should be long enough to ensure that the ineffective length will be well captured. Some studies employed RVEs with a length of between $15 \times R$ and $40 \times R$ [12, 29]. However, an RVE using these length values does not ensure a good prediction of the fibre fragmentation. A congruent RVE length depends on the fibre and matrix elastic properties as well the ineffective and debonding lengths. Thus, RVEs length with an order of magnitude equal to several times the ineffective length should be used [5, 18]. Furthermore, size effects may occur. Therefore, the RVE must be big enough to capture the micro-mechanisms of the damage, the stress redistribution around the broken fibres during the failure process, and the clusters of fibre breaks on the different planes.

The model proposed considers an RVE that contains a certain number of parallel fibres randomly allocated, with a total length L, height a, and width b. All the fibres are divided into elements of constant length l. This leads to a domain consisting of a number of *fibres* working in parallel and divided into different *planes* working in series, also known as chain of bundles [19]. The RVE may represent a hybrid, where each fibre has its own radius and properties, or a non-hybrid composite. Each fibre element is noted by the sub-indices (p, q), where p is the plane identity ranging from 1 to N_p, with N_p being the total number of planes, and q is the fibre identity ranging from 1 to N_q, with N_q being the total number of fibres. The matrix is not really represented, but it is accounted for by means of its stiffness and a shear-lag model. Fibres at the outskirts of the RVE are cut and symmetric so that the geometry obtained is completely periodic. This schema is illustrated in Figure 1. The random distribution of fibres is generated using the formulation of Melro *et al.* [30], and extended to hybrid composites by Tavares *et al.* [12].

Because of the strength scatter of the fibres, each fibre element has a different tensile strength, $\sigma_{p,q}^{\mathrm{u}}$. To do this, a random number between 0 and 1 is applied to all elements, $P_{p,q}$. Then, the strength $\sigma_{p,q}^{\mathrm{u}}$ of each element is obtained according to a statistical distribution, the element length l and $P_{p,q}$. Any statistical distribution could be adopted and implemented in the proposed model. In the literature, the Weibull distribution [31] is most commonly used to represent fibre strength, although other variants such as the bimodal and the power-law accelerated Weibull distribution are also employed [32, 33].

2.2. Constitutive equation

The model assumes the complete stress distribution on the RVE in two dependent ways. On the one hand, when a fibre breaks, shear-lag stresses are transferred between the fibre and the matrix, which can lead to debonding, matrix cracking, yielding, or a combination of these [14, 34, 35]. Consequently, an ineffective length appears so that the stress in the fibre is recovered. A shear-lag model is used to obtain the ineffective length of a broken fibre element. According to Xia *et al.* [36], shear-lag models are accurate in polymer matrix composites if the fibre stiffness is much larger than the matrix, the matrix yields and the fibre volume fraction is relatively high. Assuming that the loss of stress transfer capability produces a reduction in local effective stiffness, the shear-lag model is implemented by simply updating the damage variable of all the elements inside the ineffective length of the broken fibre. On the other hand, local stress concentration factors (*SCF*) are applied through all stress recoveries, so that the neighbouring fibres to a break are locally overloaded, increasing their failure probability. Therefore, the (*SCF*) is assumed as a dimensionless parameter equal to 1 if the fibre element is not affected by any break, or higher than 1 if it is affected by breaks. In the literature, the $SCF_{p,q}$ is measured as the ratio between the real local fibre stress, $\sigma_{p,q}$, and the fibre far field stress, $\sigma_{p,q}^{\infty}$, where the stress is not influenced by the damage, fibre breaks or stress concentration

$$\sigma_{p,q} = SCF_{p,q}\sigma_{p,q}^{\infty} \tag{1}$$

In this work, the main hypothesis is that all fibre elements in each plane work in parallel, while all planes work in series. This means that all fibre elements in the plane undergo the same deformation, ε_p, (evaluated in Section 2.4). As damage is different on each plane, a different deformation is obtained along the model. Therefore, the effective stress is given by relating the effective Young's modulus and the deformation of the plane

$$\tilde{\sigma}_{p,q} = E_q\left(1 - D_{p,q}\right)\varepsilon_p \tag{2}$$

where E_q is the Young's modulus of fibre q and $D_{p,q}$ is the state damage variable on element p, q. Therefore, the effective stress, $\tilde{\sigma}_{p,q}$, depends on the stiffness and damage distribution: the plane stiffness -by ε_p-, and the element stiffness -directly by $D_{p,q}$-, but it does not take into account the stress concentration.

To obtain the real fibre stress, $\sigma_{p,q}$, it is necessary to relate the effective stress $\tilde{\sigma}_{p,q}$,

7

and the far-field stress, $\sigma_{p,q}^{\infty}$, that appear in the definition of $SCF_{p,q}$. To do that, a stress ratio, Ω_p, is defined

$$\Omega_p = \frac{\tilde{\sigma}_{p,q}}{\sigma_{p,q}^{\infty}} \tag{3}$$

The stress ratio associated to each plane p is evaluated according to the plane level equilibrium condition explained in Section 2.4. By putting together equations (1), (2) and (3), the constitutive equation of a fibre element relates the real local longitudinal fibre stress with the longitudinal plane strain

$$\sigma_{p,q} = \frac{SCF_{p,q}}{\Omega_p} E_q \left(1 - D_{p,q}\right) \varepsilon_p \tag{4}$$

When the element's tensile stress $\sigma_{p,q}$ exceeds its strength $\sigma_{p,q}^{u}$, the element fails and its damage variable $D_{p,q}$ is set equal to 1. This causes an ineffective length in the broken fibre which is represented as damage in all the elements inside the ineffective length. Therefore, damage is equal to 0 for a pristine fibre element, equal to 1 for a broken fibre element, or between 0 and 1 for a fibre element that is influenced by the ineffective length predicted by a shear-lag model. In the following, how to evaluate $D_{p,q}$ and $SCF_{p,q}$ is explained.

The PFM is able to use any model to predict the ineffective length. In this work, the widely used Kelly-Tyson [35] shear-lag model is adopted, which assumes a perfectly plastic matrix leading to a linear stress recovery. Therefore, the ineffective length $L_{p,q}^{in}$ of a broken fibre is given by

$$L_{p,q}^{in} = \frac{E_q r_q}{2\tau_q} \varepsilon_p \tag{5}$$

where τ_q is the shear yield strength of the matrix for fibre q and r_q is the radius of fibre q. Note that both can be different for each fibre population in the case of a hybrid composite. The Kelly-Tyson model leads to different ineffective lengths depending on the elastic and geometrical properties and increases with the strain as the load is incremented.

As previously outlined, the damage variable, (calculated assuming the loss of stress transfer capability in the ineffective length), produces a reduction of local effective stiffness. Thus, a gradual decrease of damage from 1 at the position of the break, to 0 at both ends of the ineffective length (see Figure 2a and Figure 2b) is applied. As fibres may fail many times along their length, different ineffective lengths may overlap. Then, the highest damage always prevails for each element inside overlapping stress recoveries. Another

potential case is an element failure located close to the boundaries of the model. In that case, the ineffective length is not fully recovered, (see Figure 2 c). According to these hypotheses, an element p, q is affected by each break in the fibre q at each plane i with

$$
D_{p,q} = \begin{cases} \max\left(\dfrac{L_{i,q}^{\text{in}} - |i - p|\, l}{L_{i,q}^{\text{in}}}\right) & \forall i : \left(D_{i,q} = 1\right) \cup \left(|i - p|\, l < L_{i,q}^{\text{in}}\right) \\ 0 & \text{otherwise.} \end{cases} \tag{6}
$$

In general, according to the literature [29, 37, 38], the *SCF* of an affected fibre element (p, q) around a broken element (i, j) can be predicted with two interacting functions: one which depends on the radial distance between both fibres, $\delta_{(q-j)}$, and the other which depends on the plane position along the ineffective length, $\lambda_{(p-i)}$. A schematic example of the *SCF* for a fibre around a broken one is shown in Figure 3. The interaction functions $\delta_{(q-j)}$ and $\lambda_{(p-i)}$ can be parametrized with computational micro-mechanics studies (for example the work of Swolfs *et al.* [16, 18, 29, 39]), or can be formulated with analytical approaches (such as the Zhou and Wagner [37], and Eitan and Wagner [38] models). The corresponding functions are shown in Table 1.

It should be highlighted that in order to simplify the model, the widely used Kelly-Tyson shear-lag model was adopted to predict the ineffective length. Nonetheless, the *SCF* models of Eitan and Wagner and Zhou and Wagner are based on Cox's shear-lag model [34, 38] and Nayfeh's shear-lag model [37] respectively. This means that the *SCFs* are calculated using a different physical principle than the ineffective length. Nevertheless, we assume it is a reasonable approach considering the complexity involved in the process of fibre breakage. In any case, the functions to predict the *SCF* and the ineffective length are an 'exchangeable part' in the proposed Progressive Failure Model. Thus, any another model to predict the *SCF* or the ineffective length could be used instead.

Whenever different broken fibres are present, the *SCF* of an affected fibre (p, q) is obtained by assuming a linear superposition of the contribution given by all the breaks on the fibres. However, the *SCF* is bounded by the limitation of transfering load to the fibre by shear-lag. On the one hand, the elements inside any ineffective length (elements where $0 < D_{p,q} < 1$) have their stress limited by the shear-lag model. Therefore, only intact fibre elements ($D_{p,q} = 0$) can be over loaded by the *SCF*. On the other hand, another important related fact is to secure the stress continuity at the end of an ineffective length

of a broken fibre. In the last element in the ineffective length region, no *SCF* is applied, but the subsequent elements can cover part of the *SCF*. To achieve this continuity, *SCF* is limited in the elements close to ineffective length regions also in accordance with the shear-lag limitation over load transfer to the fibre. Thus, the $SCF_{p,q}$ expressed in a general form is

$$SCF_{p,q} = \begin{cases} \min\left(SCF^0_{p,q}, SCF^L_{p,q}\right) & \forall p, q : D_{p,q} = 0 \\ 1 & \text{otherwise,} \end{cases} \tag{7}$$

where $SCF^0_{p,q}$ is the *SCF* predicted by the linear superposition of the contribution of all the fibre breaks using the interacting functions as

$$SCF^0_{p,q} = 1 + \sum_{i=1}^{N_p} \sum_{j=1}^{N_q} \delta_{(q-j)} \lambda_{(p-i)} \left[D_{i,j} = 1\right] \tag{8}$$

where here [●] are the Iverson brackets and define 1 if ● is true, and 0 if it is false. $SCF^L_{p,q}$ is the *SCF* limit according to the shear-lag capacity to transfer load to the fibre, and is calculated as the slope defined by the stress gradient of the nearest ineffective length:

$$SCF^L_{p,q} = \min\left(\frac{1}{L^{\text{in}}_{i,q}} |i - p| l\right) \quad \forall i : D_{i,q} = 1 \tag{9}$$

The constitutive equation presented here allows the fibre fragmentation mechanism to be captured by means of the fibre breaks and its associated damage variable. The redistribution of stress using the shear-lag model permits several breaks along the length of any fibre. However, other mechanisms, such as delamination, are ignored by the model. Nonetheless, neglecting delamination is an acceptable assumption in the failure prediction of non-hybrids and of an intrayarn hybrid, where the different fibre populations are mixed at the fibre level. In other hybrid configurations, such as an interlayer hybrid where the different fibres are located in different layers, delamination should be considered.

2.3. Element stiffness, plane stiffness and global RVE stiffness

As previously mentioned, the proposed methodology leads to different elongations through the domain, causing a dissimilar strain for each plane ε_p. The approach proposed is to compute the strains of each plane according to the element's stiffness and the initial hypothesis that fibres work in parallel and planes in series.

The progressive failure is formulated using the stiffness damage of each fibre element,

10

$D_{p,q}$. To do so, Hooke's law of an element under tensile stress defines the longitudinal stiffness of a single fibre element, $k_{p,q}$, with

$$k_{p,q} = E_q \left(1 - D_{p,q}\right) \frac{A_q}{l} \tag{10}$$

where A_q is the cross-sectional area of fibre q given by $A_q = s_q \, \pi r_q^2$, and where s_q is a factor which guarantees the appropriate area of not entire fibres on the domain will be considered ($s_q = 1$ for entire fibres and $s_q < 1$ for fibres located at the corners, or the outskirts of the RVE).

The total stiffness of each plane can be obtained by assuming that all fibre elements in the plane and the matrix stiffness work in parallel

$$k_p = \sum_{q=1}^{N_q} k_{p,q} + E_{\mathrm{m}} \frac{A_{\mathrm{m}}}{l} \tag{11}$$

where the matrix behaviour is assumed to be linear elastic, with E_{m} being the matrix Young's modulus, and A_{m} the matrix cross-sectional area of the RVE, $A_{\mathrm{m}} = a \, b - \sum_{q=1}^{N_q} A_q$.

Similarly, the total stiffness is calculated by assuming that all planes work in series

$$K = \left(\sum_{p=1}^{N_p} \frac{1}{k_p}\right)^{-1} \tag{12}$$

2.4. External and internal equilibrium

Because of mechanical equilibrium, the internal force of each plane, F_p, must be equal to the total external force, F, sustained by the system so that $F = F_p$. The total external force can be found by relating the current total stiffness, K, and the global longitudinal homogenized strain, ε^0, given in Section 2.6. Similarly, the force of each plane can also be obtained by relating the plane stiffness and the strain of the plane leading to

$$F = F_p \qquad K \, \varepsilon^0 \, L = k_p \, \varepsilon_p \, l \tag{13}$$

Therefore, ε_p is obtained as a function of ε^0 with

$$\varepsilon_p = \frac{K \, L}{k_p \, l} \varepsilon^0 \tag{14}$$

To maintain local load equilibrium, the aggregation of the loads of the fibres and the matrix, must be equal to the load of the plane, therefore

$$F_p = k_p \, \varepsilon_p \, l = \sum_{q=1}^{N_q} \sigma_{p,q} A_q + \varepsilon_p E_{\mathrm{m}} A_{\mathrm{m}} \tag{15}$$

11

By substituting equation (4) in (15), and re-organizing, Ω_p can be found as

$$\Omega_p = \frac{\sum_{q=1}^{N_q} SCF_{p,q} E_q \left(1 - D_{p,q}\right) A_q}{k_p \, l - E_{\mathrm{m}} A_{\mathrm{m}}} \tag{16}$$

where Ω_p as result of a plane level equilibrium becomes constant to all fibre elements in plane p. An additional formulation of Ω_p is obtained by substituting (11) in (16) leading to

$$\Omega_p = \frac{\sum_{q=1}^{N_q} SCF_{p,q} E_q \left(1 - D_{p,q}\right) A_q}{\sum_{q=1}^{N_q} E_q \left(1 - D_{p,q}\right) A_q} \tag{17}$$

Once Ω_p has been evaluated, all $\sigma_{p,q}$ can be calculated from equation (4) and compared with their strength $\sigma_{p,q}^u$. It is worth mentioning that small deformations are assumed. Thus, the element length l, total RVE length L and cross-sectional areas A_q, A_{m} remain constant.

2.5. Composite homogenized stress and break density

The homogenized composite stress is obtained as an average of both element stresses and matrix stress, weighed by their volume fraction. For a non-hybrid, this leads to

$$\sigma^0 = \frac{v_{\mathrm{f}}}{N_p N_q} \sum_{p=1}^{N_p} \sum_{q=1}^{N_q} \sigma_{p,q} + \frac{1 - v_{\mathrm{f}}}{N_p} \sum_{p=1}^{N_p} E_{\mathrm{m}} \varepsilon_p \tag{18}$$

where v_{f} is the total fibre volume fraction.

For a hybrid composite, the average of the fibre stress must be calculated independently for each fibre type to capture the differences in the cross-sectional area

$$\sigma^0 = \frac{v_{\mathrm{f1}}}{N_p N_1} \sum_{p=1}^{N_p} \sum_{q \in \mathrm{f1}} \sigma_{p,q} + \frac{v_{\mathrm{f2}}}{N_p N_2} \sum_{p=1}^{N_p} \sum_{q \in \mathrm{f2}} \sigma_{p,q} + \frac{1 - v_{\mathrm{f1}} - v_{\mathrm{f2}}}{N_p} \sum_{p=1}^{N_p} E_{\mathrm{m}} \varepsilon_p \tag{19}$$

where v_{f1} and v_{f2} are the relative fibre volume fractions of each fibre population in the case of a hybrid, and N_1 and N_2 are the number of fibres in populations f1 and f2, respectively.

The break density is calculated by dividing the number of broken elements into the total RVE volume as

$$\rho_{\mathrm{b}} = \frac{1}{a \, b \, L} \sum_{p=1}^{N_p} \sum_{q=1}^{N_q} \left[D_{p,q} = 1 \right] \tag{20}$$

where $[\bullet]$ is the Iverson bracket. In the case of a hybrid composite, the break density of each population can also be calculated with the respective number of broken elements.

2.6. Algorithm procedure

A controlled monotonic increment of longitudinal displacement is performed along z direction to guarantee a stable tensile damage process. Hence, each new loading step t starts by increasing the current longitudinal displacement applied, $(u)_t$, with

$$(u)_t = (u)_{t-1} + (\Delta u)_t \tag{21}$$

where $(u)_{t-1}$ is the displacement from the previous step, and $(\Delta u)_t$ is the displacement increment. In each load step, the longitudinal displacement and the global longitudinal homogenized strain, ε^0, assuming a uni-axial behaviour, are both related by the total length of the model with

$$\left(\varepsilon^0\right)_t = \frac{(u)_t}{L} \tag{22}$$

Following this, the stiffness, forces, strains and Ω_p are first estimated with the damage variable and the *SCF* from the previous step with equations (10), (11), (12), (14) and (17). Note that, in the first step $t = 1$, all damage variables $D_{p,q}$ are equal to zero, and all $SCF_{p,q}$ are equal to one. If there are broken elements, then the ineffective length, damage variable and the *SCF* are calculated with the estimated stiffness, forces, strains and Ω_p using equations (5), (6) and (7). As the damage has changed, the stiffness, forces, strains and Ω_p are re-calculated to obtain the true actual current magnitudes. Next, the element stresses are computed with equation (4). If no elements break, the composite stress and break densities are evaluated with equations (18), (19) and (20). If new elements fail, the damage $D_{p,q}$ of all new broken elements is set equal to 1 and the same procedure is repeated without increasing the applied displacement and with the current damage and latest calculated *SCF*, until no more failures happen in the current step. When no new elements fail, a new step is started by updating $(u)_t$ and $\left(\varepsilon^0\right)_t$ with equations (21) and (22). This procedure is shown in the flowchart in Figure 4. The model stops when either all elements in a plane are damaged, or the composite stress has decreased by a pre-defined percentage of maximum load value. For non-hybrid composites, where a brittle failure is expected, the simulation is stopped when the stress decreases 10% from the maximum reached. In a hybrid composite, LE fibre population could fail originating a large load drop. To avoid an early end of the simulation before HE fibre failure, the calculation is stopped when the stress decreases more than 80%. The model was implemented in MatLab (The Math-

13

Works Inc., USA) [40] and Python programming language (Python Software Foundation, https://www.python.org/). The results can be exported into ParaView (Kitware Inc., USA) [41] for visual post-processing.

3. Results and discussion

3.1. Non-hybrid UD T700S and M40 carbon fibre epoxy

Two different non-hybrid UD composites consisting of T700S-Epoxy and M40-Epoxy were simulated using the proposed PFM. The results were compared with the reported experimental data in Swolfs *et al.* [18] and Koyanagi *et al.* [42] respectively, in an attempt to validate the model. All model properties shown in Table 2, except the estimated matrix and *SCF* related properties, were also taken from [18] and [42]. The tensile behaviour of each composite system was performed with all three models shown in Table 1 to observe their impact on the final failure. The parameters P_1 and P_2 were taken to be $P_1 = 6.12$ and $P_2 = 7.74$, as in [18].

Like [18], a bimodal Weibull distribution was applied to assign the strength, $\sigma_{p,q}^u$, to each fibre element of the T700S composite with

$$P_{p,q} = 1 - \exp\left(-\left(\frac{l}{L_0}\right)\left(\frac{\sigma_{p,q}^u}{\sigma_{01}}\right)^{m_1} - \left(\frac{l}{L_0}\right)\left(\frac{\sigma_{p,q}^u}{\sigma_{02}}\right)^{m_2}\right) \tag{23}$$

Whereas, according to [42], a traditional Weibull distribution was applied for the M40 composite using

$$P_{p,q} = 1 - \exp\left(-\frac{l}{L_0}\left(\frac{\sigma_{p,q}^u}{\sigma_0}\right)^m\right) \tag{24}$$

where $P_{p,q}$ is a random number between 0 and 1, $L_0, m, \sigma_0, \sigma_{01}, m_1, \sigma_{02}$ and m_2 are Weibull parameters and $\sigma_{p,q}^u$ is the corresponding strength of the fibre element.

A stiffening effect was assumed for the T700S composite only, to be consistent with [18]. Hence, the Young's modulus of the fibres at a step t was given as described in Toyama and Takatsubo [43]

$$\left(E_q\right)_t = E_0 + 1000\left(4133.6\left(\varepsilon^0\right)_t - 70331\left(\varepsilon^0\right)_t^2\right) \tag{25}$$

The initial Young's modulus, E_0, was chosen to be consistent with [18].

The main issue in defining the model was to decide on the appropriate width, thickness and length of the RVE. These dimensions had to be as close as possible to the real

14

specimen but still ensure that the model would be workable. To observe the influence the RVE size has on the results, RVEs of a width and thickness of $50 \times R$, $100 \times R$, $150 \times R$ and $200 \times R$ —where R is the fibre radius— were generated. Figure 5 shows a cross-section view of an example of the fibre distributions obtained.

The RVE length of the T700S was 1.54 mm for all cases, which corresponded to the length of the testing coupon [18]. However, for the M40, the experimental length was 150 mm [42], which is too long to be simulated while maintaining an appropriate small element length. Thus, a first previous study was performed with the M40 composite to determine the sensitivity of the results for both the RVE length L and the element length l. The results obtained from this analysis (Figure 6) suggested that an element length below $3 \times R$ is small enough, while an RVE length of 25 mm is acceptably long enough. Hence, the RVE length L of the M40 composite was set to 25 mm. Consequently, an element length l of 3.5×10^{-3} and 8.3×10^{-3} mm for the T700S and M40 composites, respectively, was applied. These values were taken as a compromise between accuracy and computational time.

In addition, the variability in the results caused by the randomness of fibre position and fibre strengths had to be considered. Thus, all simulations of each size and SCF model were solved 40 times with different fibre distributions, leading to a total of 480 simulations for each composite.

Considering all the inevitable inaccuracies in the modelling assumptions and in the input data, the predicted ultimate strain and strength presented remarkable agreement with the given experimental data for both the T700S and M40 composites, especially for the largest RVE sizes. For the T700S composite, the proposed PFM predicted in the largest RVE, a mean failure strain of 2.14% with the Swolfs SCF model, and of 2.07%, using the Eitan SCF and the Zhou SCF models which over-predict the experimental result of 1.89%, but are close to the 2.17% prediction of Swolfs' strength model [18]. Similarly, for the M40 composite the models predicted a mean failure strength between 2511 MPa and 2572 MPa, albeit with a small over-prediction of 2310 MPa for the experimental one as well.

The obtained failure strain and stress decreased as the RVE cross-sectional size increased; which is coherent with the size effect. These findings suggest that an RVE with a

width and thickness size of $50 \times R$ (adequate for elastic predictions according to [27, 28]) is not enough to predict unidirectional composite failure mechanisms. The error bars within the 95% confidence intervals in Figures 7 and 8, decrease with larger RVE sizes.

The size effect was remarkably less pronounced in the Swolfs *et al.* [18] *SCF* model. To better understand the differences between the *SCF* models implemented, a plot example of the predicted *SCF* with all models is shown in Figure 9. As can be seen, the Swolfs *SCF* model predicts a much larger *SCF* at a smaller centre-to-centre distance, d_{q-j}^{c}, to the broken fibre. However, the *SCF* decreases much faster by increasing, d_{q-j}^{c}, in comparison to the other models. Therefore, the Swolfs *SCF* model is more localized than the others. This should explain why the size effect is smaller with the Swolfs model: causing *SCF* in a smaller centre-to-centre distance means that fewer fibres are needed to accurately represent stress re-distribution around fibre breaks. The Zhou and Wagner and Eitan and Wagner *SCF* models both estimate the same stress peak, but the *SCF* along the ineffective length is different. For the Eitan and Wagner model, the *SCF* distribution along the ineffective length is narrower and affects only a small region of the intact fibres close to the broken fibre. By increasing d_{q-j}^{c}, the *SCF* distribution along the ineffective length tends to coincide with the Zhou and Wagner model.

The cluster evolutions, with the T700S composite for each *SCF* model, are shown at different instants close to final failure in Figure 10. It can be observed that groups of clusters formed with all models. These clusters increased in size as the load was incremented until a critical cluster propagated and led to final failure. Even though the same fibre strengths were used with all three *SCF* models, the failure procedure was clearly different. Not only was the failure strain different, but so too were the clusters formed at the different places in the model. Moreover, final failure, due to unstable cluster propagation, also happened at a different location.

By observing the results obtained, it is not possible to conclude if an *SCF* approach is more accurate than the others. Indeed, the results show that the *SCF* model has only a relative influence on the predicted failure. The significant difference between the *SCF* models analysed is the formulation basics and the nature of the identification parameters. The Zhou and Wagner model and the Eitan and Wagner model are formulations totally based on theoretical shear-lag assumptions. These models need a major number of pa-

rameters, which are not always simple to estimate, such as ψ or r_{m}. However, the Swolfs *SCF* model proposes a completely different approach, by where the *SCF* is obtained by fitting results from a micro-mechanic finite element analysis using a relatively large RVE with hundreds of fibres and a long length.

Both composites presented a different failure. The T700S composite experimented some stiffness loss before final failure, whereas the M40 composite exhibited a very brittle failure, as seen in Figures 11a and 12a. This effect is highlighted by the evolution of the break densities in Figures 11b and 12b, as the curve of the M40 presents a more sudden degradation than that of T700S. The break density of T700S was over-predicted by the model compared to the experimental results, as in Swolfs *et al.* [18], which could be the consequence of inaccuracies in the model or in the experimental data. A summary of the results obtained is presented in Table 3. The total computational time is also shown for each set of simulations and presented a strong exponential increase by increasing the width/thickness of the RVE. The simulations using the Swolfs *SCF* model needed smaller computational time in the PFM. However, it must be remarked that the two constants (P_1 and P_2) used by this *SCF* model are obtained from micromechanical finite element analyses which represent a considerable effort.

3.2. Hybrid UD AS4-M50S carbon fibres/epoxy

A UD intrayarn hybridization within M50S carbon (LE fibre) and AS4 Carbon (HE fibre) with epoxy matrix was simulated at different LE relative hybrid volume fractions. All data, shown in Table 2, was taken from Tavares *et al.* [12]. In order to carry out a clean comparison with [12] FEM results, the simulations were performed using the same RVE dimensions. Thus, RVEs with width, thickness and length of $15 \times R$ were generated, with R being the largest fibre radius in the RVE. It is important to remark that while such a small RVE is not big enough to properly represent the failure process accurately, it is the appropriate configuration to compare the PFM simulation with the micro-mechanical FEM results. A Weibull distribution extrapolated to the total gauge length (instead of the element length) was also used:

$$P_{p,q} = 1 - \exp\left(-\frac{L}{L_0}\left(\frac{\sigma_{p,q}^u}{\sigma_0}\right)^m\right) \tag{26}$$

where the element length L was set to 0.35×10^{-3} mm.

17

The *SCF* model used was from Swolfs *et al.* [18]. In a hybrid composite the appropriate *SCFs* profiles depend on the stiffness ratio between the broken and the intact fibre (E_j/E_q). Three combination cases are then possible: i) a broken LE fibre causing *SCF* to an HE fibre ($E_j/E_q = 2.05$), ii) a broken HE fibre causing *SCF* to an LE fibre ($E_j/E_q = 0.49$), and iii) a broken fibre (LE or HE) causing *SCF* to a fibre of the same population ($E_j/E_q = 1$). Swolfs *et al.* [39] provided the *SCF* for $E_j/E_q = 3.71$ and $E_j/E_q = 1.85$. Thus, interpolation and extrapolation was performed in between to obtain the *SCF* for $E_j/E_q = 2.05$ and $E_j/E_q = 0.49$, respectively. These profiles are shown in Figure 13a. When either a broken LE fibre causes *SCF* to an intact LE, or a broken HE fibre causes *SCF* to an intact HE fibre, the profile shown in Figure 13b was assumed, which was also taken from [39]. Thus, the corresponding parameters P_1 and P_2 from Table 1 are $P_1 = 2.982, P_2 = 3.068$ for $E_j/E_q = 3.71$, $P_1 = 1.908, P_2 = 1.975$ for $E_j/E_q = 1.85$, and $P_1 = 3.656, P_2 = 3.053$ for the *SCF* profile between fibres of the same population. Note that for the two non-hybrid cases (a 100% HE composite and a 100% LE composite), the same Swolfs *et al.* [18] *SCF* model used in Section 3.1 was applied. Moreover, it is worth mentioning that the stress re-distribution between fibres of the same type (Figure 13b), which share the same stiffness and radius, differs from the one obtained between fibres of different type (Figure 13a), with distinct stiffness and fibre radii. Therefore, the *SCF* for $E_j/E_q = 1$ does not fit in between the curves of $E_j/E_q = 0.49$ and $E_j/E_q = 1.85$.

Within each hybrid relative volume fraction modelled (see Figure 14), 40 simulations were solved leading to a total of 360 simulations, with each set of 40 simulations taking approximately 9 minutes to be completed. The tensile stress-strain curves obtained are shown and compared with the [12] FEM results in Figure 14 at LE hybrid volume fractions of 0, 25, 50, 75 and 100%. A good agreement was obtained, which led to similar failure responses.

Pseudo-ductility was predicted at LE relative volume fractions between 10 and 30%. The other composites either failed prematurely, or the interaction between fibres was not evident enough. This failure process is highlighted in Figure 15. For nearly all the hybrid configurations it is possible to observe that the LE fibre break density does not increase once a certain point is reached. That means that the LE fibre is fully fragmented and is incapable of breaking further, even when the applied load is incremented. At low LE

volume fractions between 10 and 30%, the breaks of the LE fibre saturated while the HE fibre was failing, which led to pseudo-ductility until the final failure. However, at higher LE volume fractions the failure was sudden and brittle. These results demonstrate that the proposed model is able to capture fibre fragmentation, which is one of the most relevant mechanisms associated to pseudo-ductility.

The hybrid failure strain is also presented in Figure 16. For LE volume fractions lower than 70%, the hybrid failure strain was considered as the corresponding strain at the second maximum in the stress-strain curve, which corresponded to the failure of the HE fibre in the hybrid. However, for larger LE volume fractions, the first maximum was considered as failure strain instead, because the drop in stress afterwards did not show any evidence of a second maximum. These failure strain values correspond to the failure of the LE fibres.

The small discrepancies between PFM and FEM are attributed to the shear-lag model, the prediction of *SCF* and, in particular, the omission of dynamic phenomena. Nonetheless, the proposed model predicted similar results using a very simple model that can be run on a regular computer in a short time, whereas Tavares *et al's* [12] model requires an enormous computational effort in a high power computational facility.

Future work should try to address the problems omitted here such as matrix damage, thermal residual stresses and dynamic effects. Further parametric studies to design hybrid configurations to maximise pseudo-ductility and the effect of unknown parameters such as the effect of debonding or the effect of the size in the hybrid effect should also be included.

4. Conclusions

A 3D progressive failure model based on the chain of bundles approach [19], was developed and validated. The model accurately represents the failure curve of unidirectional composite materials with a random distribution of fibres. A complete stress distribution is obtained by associating a damage variable to the loss of stress transfer capability along the ineffective length, which produces a reduction of local effective stiffness. Consequently, local stress concentrations are applied through all stress recoveries, so that the neighbouring fibres are locally overloaded. The method, formulated in an explicit form, leads to

19

different deformations along the length of the model.

The model has been validated with results available in the literature. Each simulation, with different random distribution of fibres, has been repeated multiple times to evaluate the uncertainly of the results. For non-hybrids, T700S-Epoxy and M40-Epoxy UD composites were simulated and compared to results from Swolfs *et al.* [18] and Koyanagi *et al.* [42], respectively. Moreover, an RVE size with transversal dimensions larger than $200 \times R$ is needed to capture the size effect inherent to the failure process, which is more exigent than the required $50 \times R$ for elastic RVE predictions according to [27, 28]. Three *SCF* models corresponding to the models of Swolfs *et al.* [18], Zhou and Wagner [37] and Eitan and Wagner [38] were compared and found to have a slightly different failure prediction. A significant difference between these formulations is the parameters identification method. The Zhou and Wagner model and the Eitan and Wagner model are entirely based on theoretical assumptions. They need a significant number of parameters and some of them are not easy to calculate or estimate. Meanwhile, the Swolfs *SCF* model is parametrized with a simpler set of values. The exact identification of these must be performed by a micro-mechanical finite element approach. However, all three models led to a similar failure procedure which showed a tendency to form clusters of broken fibres and which led to final failure. In any case, the Swolfs *SCF* model generates more localized stress concentration factors, leading to predictions significantly less sensitive to the size effect when compared to the other models. Finally, a hybrid carbon-carbon (M50S-AS4) epoxy composite was simulated and pseudo-ductility was obtained at LE volume fractions between 10 and 30%. The results were compared with those of Tavares *et al.* [12] micro-mechanical FEM and also obtained good agreement, but with a much faster and simpler model than the FEM is.

Acknowledgments

References

[1] A. Turon, J. Costa, P. Maimí, D. Trias, J. A. Mayugo, A progressive damage model for unidirectional fibre-reinforced composites based on fibre fragmentation. Part I: Formulation, Composites Science and Technology 65 (13) (2005) 2039–2048. doi:10.1016/j.compscitech.2005.04.012.

[2] Y. Swolfs, L. Gorbatikh, I. Verpoest, Fibre hybridisation in polymer composites: A review, Composites Part A: Applied Science and Manufacturing 67 (2014) 181–200. doi:10.1016/j.compositesa.2014.08.027.

[3] Y. Swolfs, I. Verpoest, L. Gorbatikh, Maximising the hybrid effect in unidirectional hybrid composites, Materials and Design 93 (2016) 39–45. doi:10.1016/j.matdes.2015.12.137.

[4] G. Czél, M. Jalalvand, M. R. Wisnom, Design and characterisation of advanced pseudo-ductile unidirectional thin-ply carbon/epoxy-glass/epoxy hybrid composites, Composite Structures 143 (2016) 362–370. doi:10.1016/j.compstruct.2016.02.010.

[5] Y. Swolfs, R. M. McMeeking, I. Verpoest, L. Gorbatikh, The effect of fibre dispersion on initial failure strain and cluster development in unidirectional carbon/glass hybrid composites, Composites Part A: Applied Science and Manufacturing 69 (2014) 279–287. doi:10.1016/j.compositesa.2014.12.001.

[6] J. Xing, G. Hsiao, T.-W. Chou, A Dynamic Explanation of The Hybrid Effect, Journal of Composite Materials 15 (5) (1981) 443–461. doi:10.1177/002199838101500504.

[7] Y. Swolfs, I. Verpoest, L. Gorbatikh, A review of input data and modelling assumptions in longitudinal strength models for unidirectional fibre-reinforced composites, Composite Structures 150 (2016) 153–172. doi:10.1016/j.compstruct.2016.05.002.

[8] M. R. Wisnom, G. Czel, Y. Swolfs, M. Jalalvand, L. Gorbatikh, I. Verpoest, Hybrid effects in thin ply carbon/glass unidirectional laminates: Accurate experimental determination and prediction, Composites Part A: Applied Science and Manufacturing 88 (2016) 131–139. doi:10.1016/j.compositesa.2016.04.014.

[9] T. Hayashi, On the improvement of mechanical properties of composites by hybrid composition, in: Proc 8th Int Reinforced plastics Conference, 1972, pp. 149–152.

[10] C. Zweben, Tensile strength of hybrid composites, Journal of Materials Science 12 (7) (1977) 1325–1337. doi:10.1007/BF00540846.

[11] H. Fukuda, An advanced theory of the strength of hybrid composites, Journal of Materials Science 19 (3) (1984) 974–982. doi:10.1007/BF00540468.

[12] R. P. Tavares, A. R. Melro, M. A. Bessa, A. Turon, W. K. Liu, P. P. Camanho, Mechanics of hybrid polymer composites: analytical and computational study, Computational Mechanics 57 (3) (2016) 405–421. doi:10.1007/s00466-015-1252-0.

[13] A. R. Melro, P. P. Camanho, F. M. Andrade Pires, S. T. Pinho, Micromechanical analysis of polymer composites reinforced by unidirectional fibres: Part I-Constitutive modelling, International Journal of Solids and Structures 50 (11-12) (2013) 1897–1905. doi:10.1016/j.ijsolstr.2013.02.009.

[14] T. Okabe, N. Takeda, Y. Kamoshida, M. Shimizu, W. A. Curtin, A 3D shear-lag model considering micro-damage and statistical strength prediction of unidirectional fiber-reinforced composites, Composites Science and Technology 61 (12) (2001) 1773–1787. doi:10.1016/S0266-3538(01)00079-3.

[15] T. Okabe, H. Sekine, K. Ishii, M. Nishikawa, N. Takeda, Numerical method for failure simulation of unidirectional fiber-reinforced composites with spring element model, Composites Science and Technology 65 (6) (2005) 921–933. doi:10.1016/j.compscitech.2004.10.030.

[16] Y. Swolfs, R. M. McMeeking, I. Verpoest, L. Gorbatikh, Matrix cracks around fibre breaks and their effect on stress redistribution and failure development in uni-

directional composites, Composites Science and Technology 108 (2015) 16–22. doi:10.1016/j.compscitech.2015.01.002.

[17] Y. Swolfs, I. Verpoest, L. Gorbatikh, Issues in strength models for unidirectional fibre-reinforced composites related to Weibull distributions, fibre packings and boundary effects, Composites Science and Technology 114 (2015) 42–49. doi:10.1016/j.compscitech.2015.04.002.

[18] Y. Swolfs, H. Morton, A. E. Scott, L. Gorbatikh, P. A. S. Reed, I. Sinclair, S. M. Spearing, I. Verpoest, Synchrotron radiation computed tomography for experimental validation of a tensile strength model for unidirectional fibre-reinforced composites, Composites Part A: Applied Science and Manufacturing 77 (2015) 106–113. doi:10.1016/j.compositesa.2015.06.018.

[19] B. W. Rosen, Tensile failure of fibrous composites, AIAA Journal 2 (11) (1964) 1985–1991. doi:10.2514/3.2699.

[20] H. Fukuda, Micromechanical strength theory of hybrid composites, Advanced Composite Materials 1 (1) (1991) 39–53. doi:10.1163/156855191X00054.

[21] W. Fang, W. Yuqing, C. Zhiqian, Micromechanical modeling of the effect of progressive damage on the tensile behavior in fiber-reinforced polymer composites, Advanced Materials Research 79-82 (2009) 1347–1350. doi:10.4028/www.scientific.net/AMR.79-82.1347.

[22] G. Czél, M. R. Wisnom, Demonstration of pseudo-ductility in high performance glass/epoxy composites by hybridisation with thin-ply carbon prepreg, Composites Part A: Applied Science and Manufacturing 52 (2013) 23–30. doi:10.1016/j.compositesa.2013.04.006.

[23] H. Yu, M. L. Longana, M. Jalalvand, M. R. Wisnom, K. D. Potter, Pseudo-ductility in intermingled carbon/glass hybrid composites with highly aligned discontinuous fibres, Composites Part A: Applied Science and Manufacturing 73 (2015) 35–44. doi:10.1016/j.compositesa.2015.02.014.

[24] M. Jalalvand, G. Czel, M. R. Wisnom, Damage analysis of pseudo-ductile thin-ply UD hybrid composites - A new analytical method, Composites Part A: Applied Science and Manufacturing 69 (2015) 83–93. doi:10.1016/j.compositesa.2014.11.006.

[25] M. Fotouhi, M. Jalalvand, M. R. Wisnom, High performance quasi-isotropic thin-ply carbon/glass hybrid composites with pseudo-ductile behaviour in all fibre orientations, Composites Science and Technology 152 (2017) 101–110. doi:10.1016/j.compscitech.2017.08.024.

[26] G. Czél, M. Jalalvand, M. R. Wisnom, Design and characterisation of advanced pseudo-ductile unidirectional thin-ply carbon/epoxy-glass/epoxy hybrid composites, Composite Structures 143 (2016) 362–370. doi:10.1016/j.compstruct.2016.02.010.

[27] D. Trias, J. Costa, A. Turon, J. E. Hurtado, Determination of the critical size of a statistical representative volume element (SRVE) for carbon reinforced polymers, Acta Materialia 54 (13) (2006) 3471–3484. doi:10.1016/j.actamat.2006.03.042.

[28] J. Zangenberg, P. Brøndsted, Determination of the minimum size of a statistical representative volume element from a fibre-reinforced composite based on point pattern statistics, Scripta Materialia 68 (7) (2013) 503–505. doi:10.1016/j.scriptamat.2012.11.032.

[29] Y. Swolfs, L. Gorbatikh, V. Romanov, S. Orlova, S. V. Lomov, I. Verpoest, Stress concentrations in an impregnated fibre bundle with random fibre packing, Composites Science and Technology 74 (2013) 113–120. doi:10.1016/j.compscitech.2012.10.013.

[30] A. R. Melro, P. P. Camanho, S. T. Pinho, Generation of random distribution of fibres in long-fibre reinforced composites, Composites Science and Technology 68 (9) (2008) 2092–2102. doi:10.1016/j.compscitech.2008.03.013.

[31] W. Weibull, A statistical distribution function of wide applicability, ASME Journal (1952) 293–297.

[32] D. G. Harlow, S. L. Phoenix, Probability distributions for the strength of composite

materials II: A convergent sequence of tight bounds, International Journal of Fracture 17 (6) (1981) 601–630. doi:10.1007/BF00681559.

[33] A. S. Watson, R. L. Smith, An examination of statistical theories for fibrous materials in the light of experimental data, Journal of Materials Science 20 (9) (1985) 3260–3270. doi:10.1007/BF00545193.

[34] H. Cox, The elasticity and strength of paper and other fibrous materials, British Journal of Applied Physics 3 (3) (1952) 72–79. doi:10.1088/0508-3443/3/3/302.

[35] Kelly A., W. Tyson, Tensile properties of fibre-reinforced and metals: copper/tungsten and copper/molybdenum, Journal of the mechanics and physics of solids 13 (6) (1965) 329–350. doi:10.1016/0022-5096(65)90035-9.

[36] Z. Xia, T. Okabe, W. A. Curtin, Shear-lag versus finite element models for stress transfer in fiber-reinforced composites, Composites Science and Technology 62 (9) (2002) 1141–1149. doi:10.1016/S0266-3538(02)00072-6.

[37] X. F. Zhou, H. D. Wagner, Stress concentrations caused by fiber failure in two-dimensional composites, Composites Science and Technology 59 (7) (1999) 1063–1071. doi:10.1016/S0266-3538(98)00145-6.

[38] A. Eitan, H. D. Wagner, Fiber interactions in two-dimensional composites, Applied Physics Letters 58 (10) (1991) 1033–1035. doi:10.1063/1.105209.

[39] Y. Swolfs, L. Gorbatikh, I. Verpoest, Stress concentrations in hybrid unidirectional fibre-reinforced composites with random fibre packings, Composites Science and Technology 85 (2013) 10–16. doi:10.1016/j.compscitech.2013.05.013.

[40] U. S. The MathWorks, Inc., Natick, Massachusetts, MATLAB and Statistics Toolbox Release 2013a.

[41] J. Ahrens, B. Geveci, C. Law, ParaView: An End-User Tool for Large Data Visualization, in: Visualization Handbook, Visualization Handbook, Elsevier, 2005, pp. 717–731. doi:10.1016/B978-012387582-2/50038-1.

[42] J. Koyanagi, H. Hatta, M. Kotani, H. Kawada, A Comprehensive Model for Determining Tensile Strengths of Various Unidirectional Composites, Journal of Composite Materials 43 (18) (2009) 1901–1914. doi:10.1177/0021998309341847.

[43] N. Toyama, J. Takatsubo, An investigation of non-linear elastic behavior of CFRP laminates and strain measurement using Lamb waves, Composites Science and Technology 64 (16) (2004) 2509–2516. doi:10.1016/j.compscitech.2004.05.007.

List of Figures

Figure 1: Schema of the RVE for the Progressive Failure Model. The enumeration of the planes is sorted from 1 to N_p, with plane 1 always being the plane to the extreme right and plane N_p to the extreme left. Fibre numeration is random from 1 to N_q.
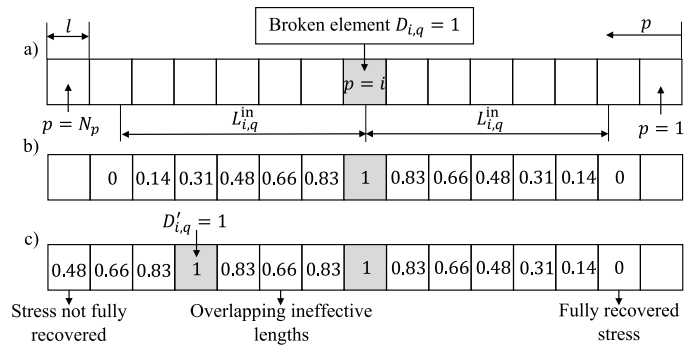
Figure 2: a) Schema of the ineffective length around a broken element, b) resultant damage distribution, c) overlapping ineffective lengths and not fully-recovered stresses in a fibre with two breaks.
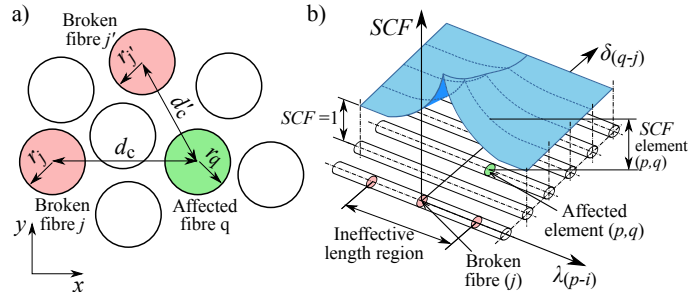
Figure 3: a) In-plane separation between broken and affected fibre, b) stress concentration schema for intact fibres around a broken fibre depending on the in-plane distance and the position along the ineffective length.
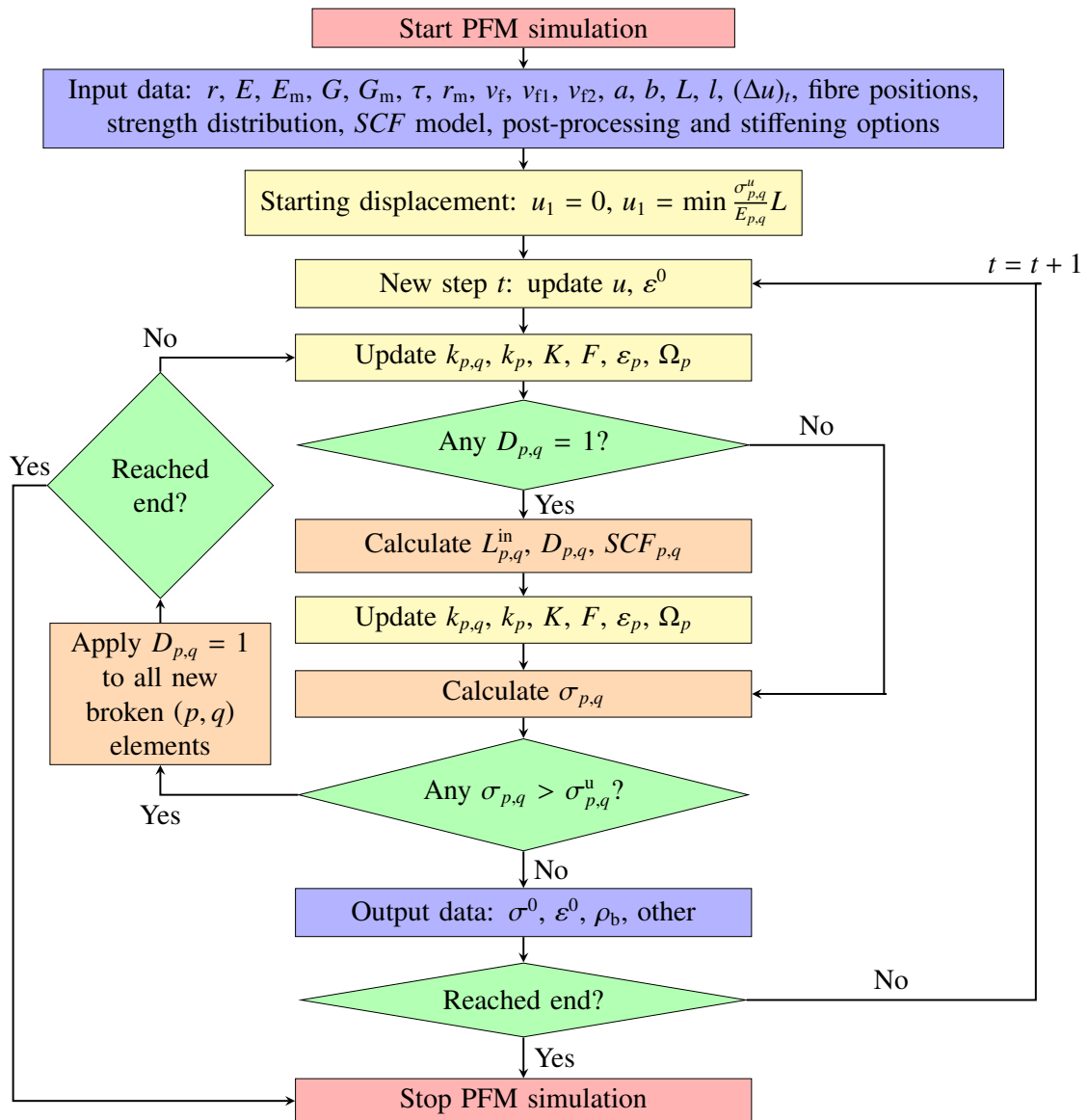
Figure 4: Progressive Failure Model flowchart.
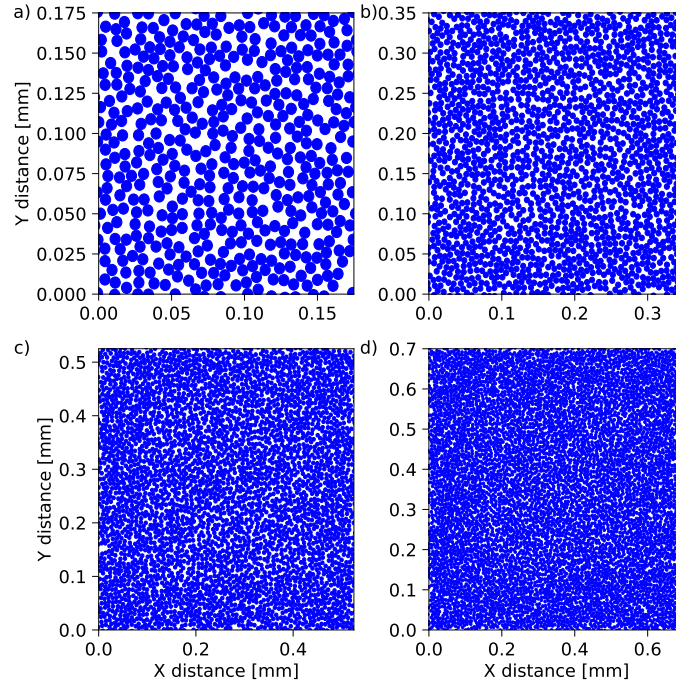
Figure 5: Cross-section view examples of RVEs with T700S fibre a) 50×R, b) 100×R, c) 150×R, d) 200×R.
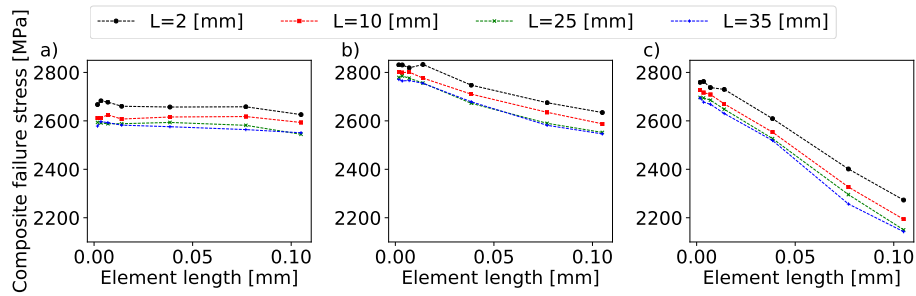
Figure 6: Influence of the total RVE length (L) and element length (l) on the failure strength for the M40 composite. The mean result for 20 simulations is shown. The RVE width and thickness were 50×R. a) Using the Swolfs *et al.* *SCF* model, b) using the Eitan and Wagner *SCF* model, and c) using the Zhou and Wagner *SCF* model.
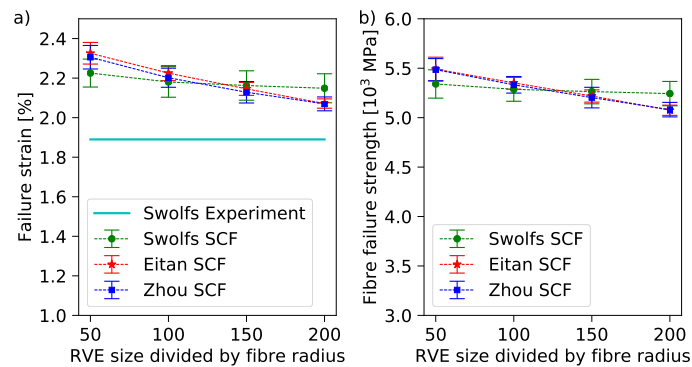

Figure 7: T700S error bars for 40 simulations at each simulated RVE size for each *SCF* model compared with Swolfs *et al.* [18] experimental results, a) failure strain, b) fibre failure stress.
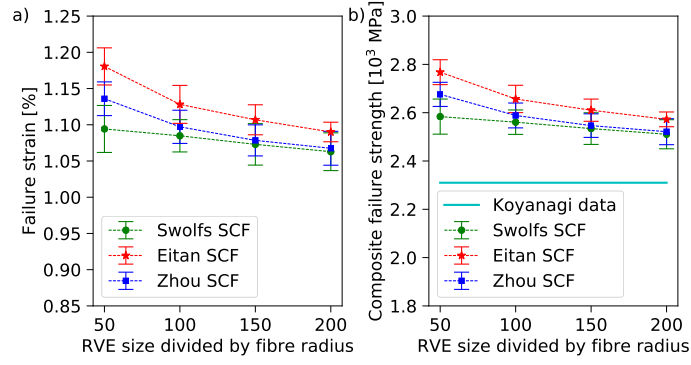
Figure 8: M40 error bars for 40 simulations for each simulated RVE size for each *SCF* model compared with Koyanagi *et al.* [42] experimental results, a) failure strain, b) composite failure stress.
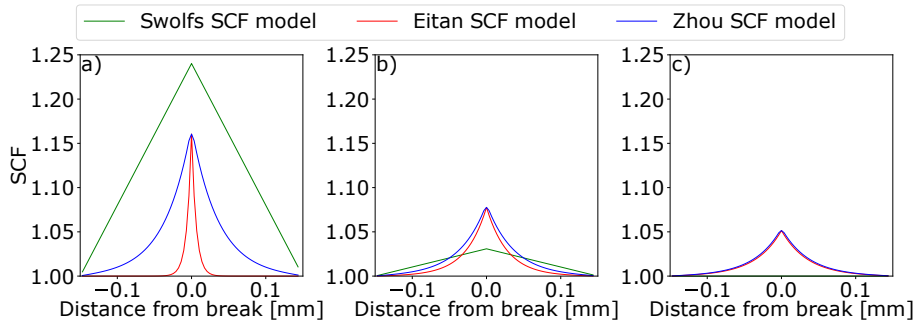

Figure 9: Predicted *SCF* to an intact fibre at different centre-to-centre distances, d^{c}_{q-j}, according to the Zhou and Wagner, Eitan and Wagner and Swolfs *et al.* models. a) $d^{c}_{q-j} = 2.07r$, b) $d^{c}_{q-j} = 4.14r$, c) $d^{c}_{q-j} = 6.21r$. The *SCF* is shown along the ineffective length of a 0.15 mm broken fibre, with all material data corresponding to the T700S fibre in Table 2.
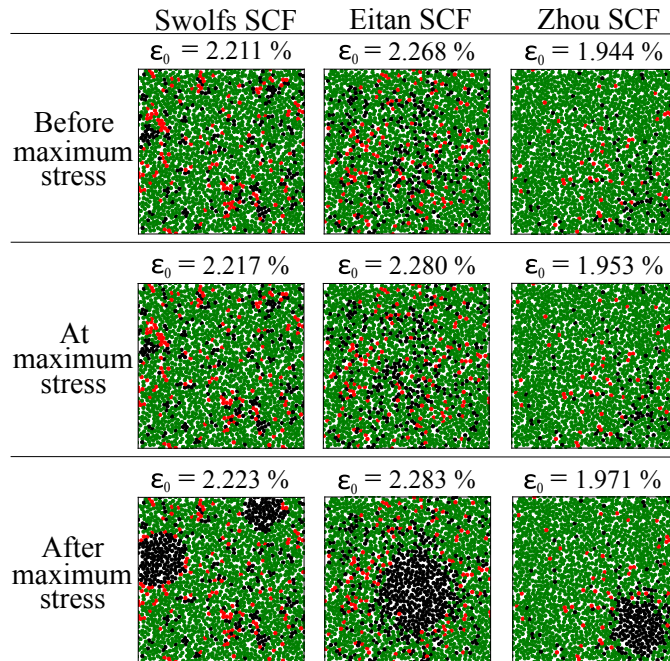
Figure 10: Cluster evolution at different stages during final failure within 16% of total length in each direction of the section with largest break density for the T700S composite. Broken fibres in black, damaged fibres in red and intact fibres in green. RVE size corresponds to $100{\times}R$.
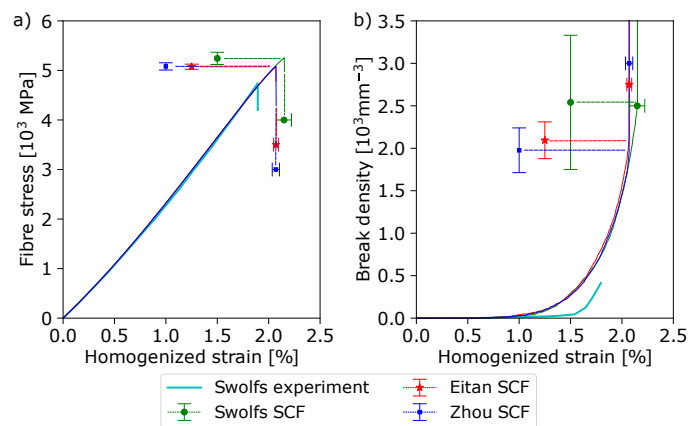

Figure 11: T700S closest curve to the mean from all 40 simulations with a size of $200{\times}R$ for each *SCF* model compared against the experimental results from Swolfs *et al.* [18], a) mean stress-strain curve, b) mean break density curve.
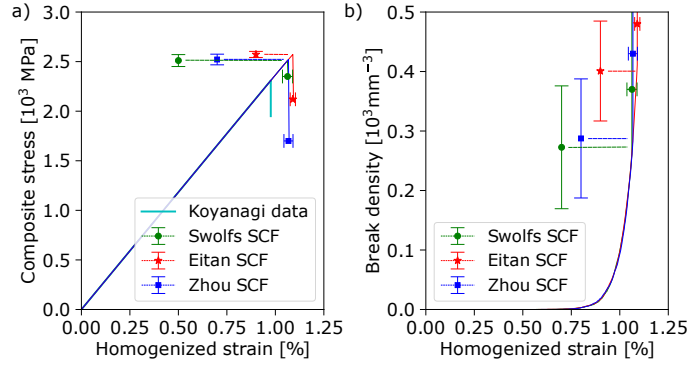
Figure 12: M40 closest curve to the mean from all 40 simulations of size $200 \times R$ for each *SCF* model compared against the experimental results from Koyanagi *et al.* [42], a) mean stress-strain curve, b) mean break density curve. The experimental stress-strain curve was assumed to be linear from the experimental strength with Young's modulus given by the rule of mixtures.
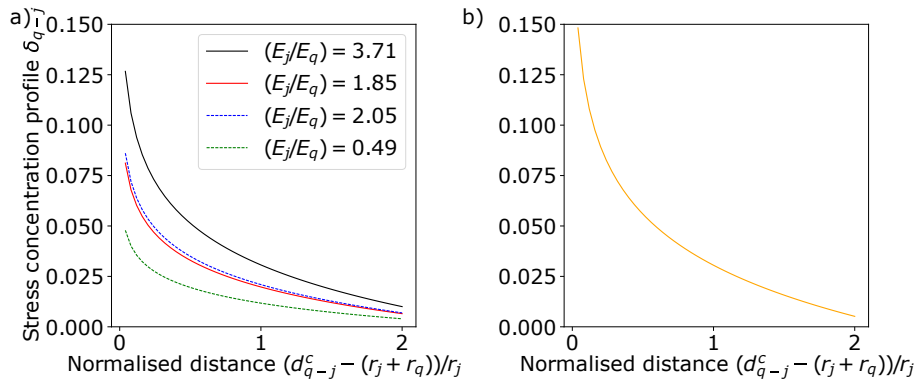

Figure 13: Hybrid stress concentration profiles. a) for different ratios E_j/E_q between broken and intact fibres when both fibres belong to different fibre populations, b) for the same fibre population.
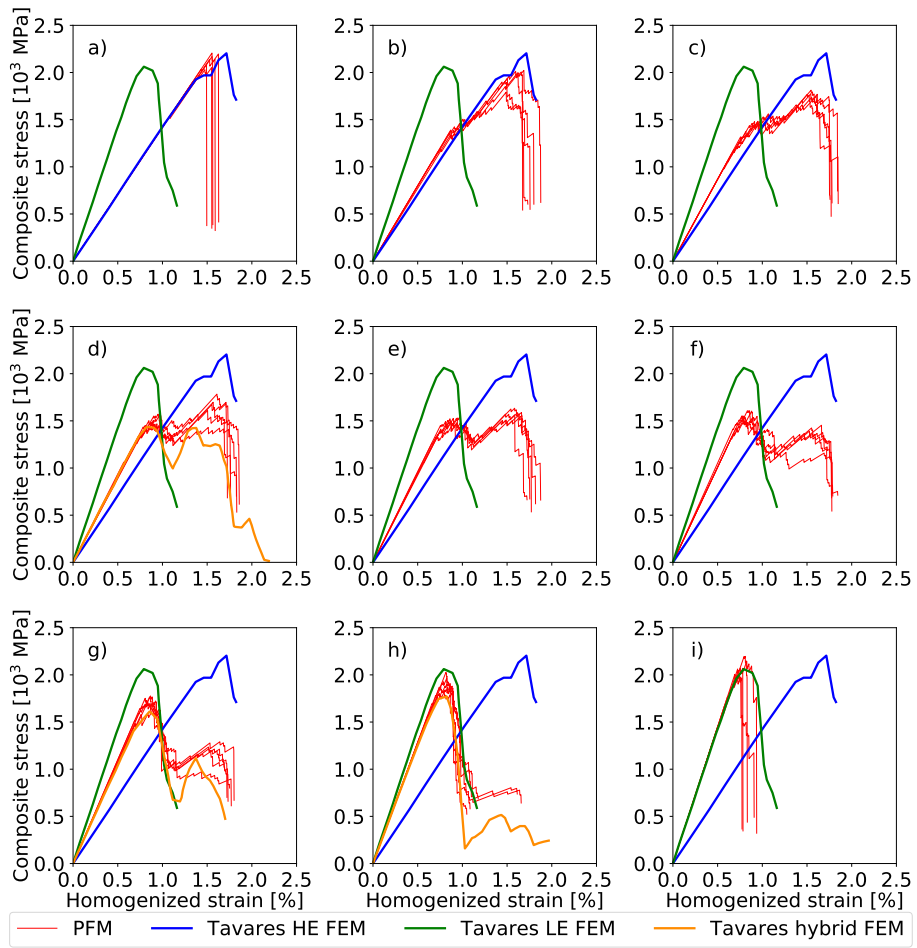
34

Figure 14: Stress-strain curves obtained for hybrid M50S-AS4 fibre compared with Tavares *et al.* [12] FEM when varying the relative LE hybrid fibre volume fraction. a) 0%LE, b) 10%LE, c) 20%LE, d) 25%LE, e) 30%LE, f) 40%LE, g) 50%LE, h) 75%LE, i) 100%LE. For the sake of readability only 5 realisations are shown.
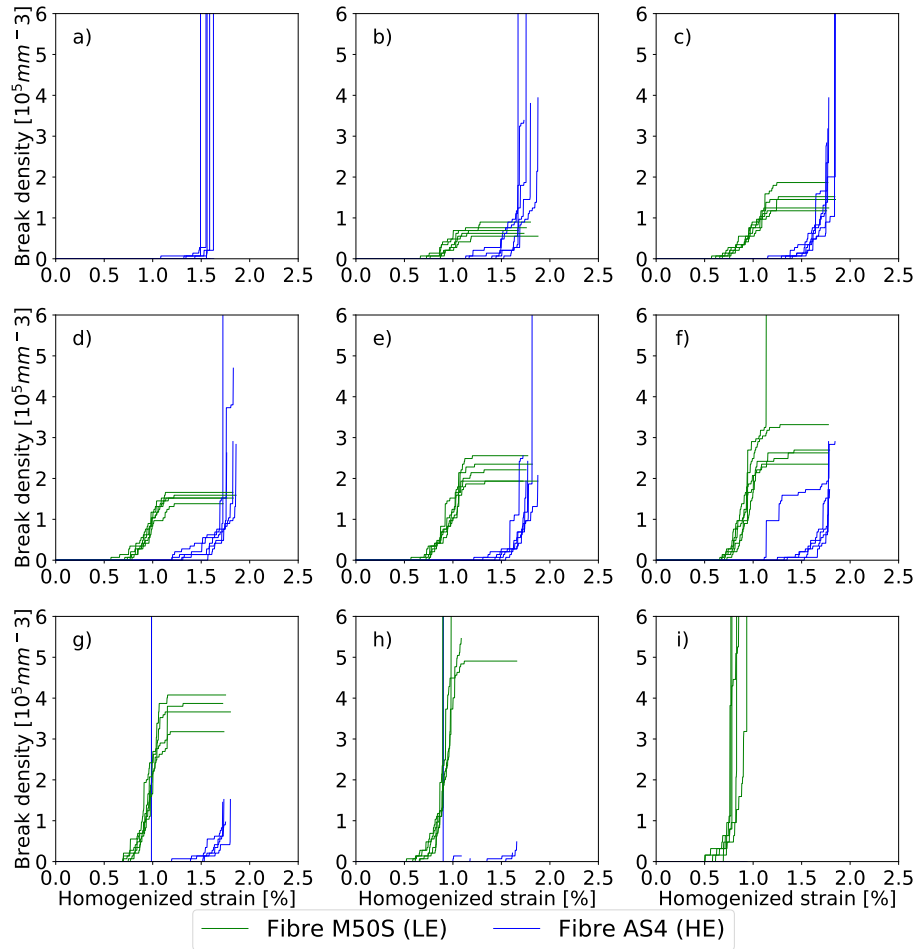
Figure 15: Break density-strain curves obtained for hybrid M50S-AS4 fibre composite when varying the relative hybrid fibre volume fraction. a) 0%LE, b) 10%LE, c) 20%LE, d) 25%LE, e) 30%LE, f) 40%LE, g) 50%LE, h) 75%LE, i) 100%LE. For the sake of readability only 5 realisations are shown.
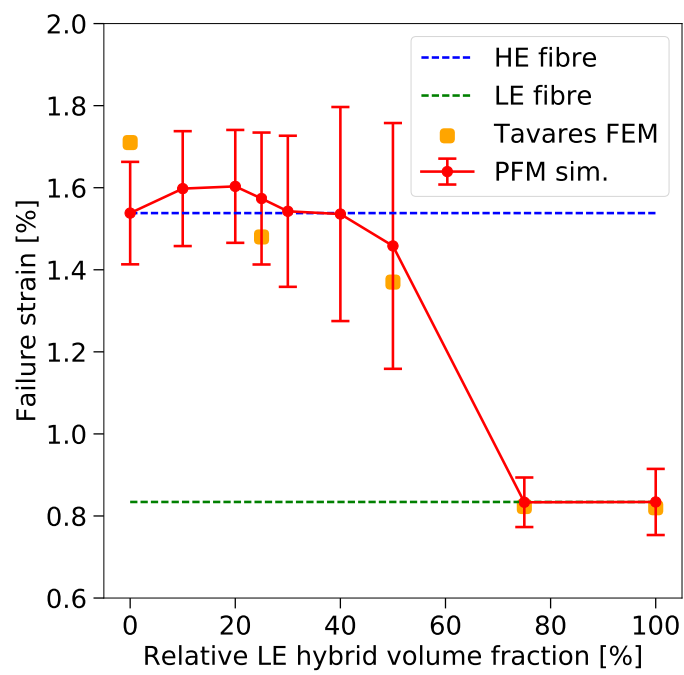
Figure 16: Hybrid failure strain obtained for different LE and HE relative volume fractions. The results of the simulations are compared with [12] FEM results. The error bars are shown within the 95% confidence intervals for 40 realizations.

List of Tables

SCF model	Functions: radial distance $\delta_{(q-j)}$ and ineffective length $\lambda_{(p-i)}$
Swolfs *et al.* [18] (∗)	$\delta_{(q-j)} = -P_1 \ln\left(\dfrac{d_{q-j}^{\mathrm{c}} - \left(r_j + r_q\right)}{r_j}\right) + P_2$ where P_1 and P_2 are two constants from a micro-mechanic model and d_{q-j}^{c} is the centre-to-centre distance between fibres q and j $\lambda_{(p-i)} = \dfrac{L_{i,j}^{\mathrm{in}} - l\,|i - p|}{L_{i,j}^{\mathrm{in}}} \quad \forall(i,j) : l\,|i - p| < L_{i,j}^{\mathrm{in}}$
Eitan and Wagner [38]	$\delta_{(q-j)} = \dfrac{\varphi_j}{\pi}$ where $\varphi_j = \arcsin\left(r_j/d_{q-j}^{\mathrm{c}}\right)$ $\lambda_{(p-i)} = \dfrac{\sinh\beta_{(q-j)}^{c}\left(L_{i,j}^{\mathrm{in}} - l\,|i - p|\right)}{\sinh\beta_{(q-j)}^{c}L_{i,j}^{\mathrm{in}}} \quad \forall(i,j) : l\,|i - p| < L_{i,j}^{\mathrm{in}}$ where $\beta_{(q-j)}^{c}$ is Cox's [34] shear-lag parameter: $\beta_{(q-j)}^{c} = \dfrac{1}{r_j}\sqrt{\dfrac{2G_{\mathrm{m}}}{E_j \ln \dfrac{0.5 d_{q-j}^{\mathrm{c}}}{r_j}}}$ where G_{m} is the matrix shear modulus.
Zhou and Wagner [37] (∗∗)	$\delta_{(q-j)} = \left(1 - \dfrac{\psi l}{r_j}\right)\dfrac{2\varphi_j}{\pi}$ where ψ is a friction coefficient $\lambda_{(p-i)} = \dfrac{\sinh\beta_j\left(L_{i,j}^{\mathrm{in}} + 0.5l - l\,|i - p|\right)}{\sinh\beta_j L_{i,j}^{\mathrm{in}}} \quad \forall(i,j) : l\,|i - p| < L_{i,j}^{\mathrm{in}}$ where β_j is Nayfeh's shear-lag parameter, as given in [37]: $\beta_j^2 = \dfrac{2}{r_j^2 E_j E_{\mathrm{m}}}\left(\dfrac{E_j \frac{r_j^2}{r_{\mathrm{m}}^2} + E_{\mathrm{m}}\left(1 - \frac{r_j^2}{r_{\mathrm{m}}^2}\right)}{\frac{1}{4G_j}\left(1 - \frac{r_j^2}{r_{\mathrm{m}}^2}\right) + \frac{1}{2G_{\mathrm{m}}}\left(\frac{r_{\mathrm{m}}^2}{r_{\mathrm{m}}^2 - r_j^2}\ln\left(\frac{r_{\mathrm{m}}^2}{r_j^2}\right) - \frac{1}{2}\left(3 - \frac{r_j^2}{r_{\mathrm{m}}^2}\right)\right)}\right)$ where G_j and r_{m} are the broken fibre shear modulus and the radius of the shear-carrying matrix cylinder

Table 1: Functions to obtain the stress concentration factor according to three different models. (∗) Swolfs *et al.* [18] function along the ineffective length has been assumed. (∗∗) Zhou and Wagner [37] provided equations for debonding and non-debonding regions. Here, only non-debonding regions are considered.

Table 2:

Composite	Fibre properties			Weibull properties			Matrix properties			*SCF* properties		RVE data	
	E, E_0 [GPa]	G [GPa]	r [mm]	m [–]	σ_0 [MPa]	L_0 [mm]	E_m [GPa]	G_m [GPa]	τ [MPa]	r_m [mm]	ψ [–]	L [mm]	v_f [%]
T700S-Epoxy	197.9	78.53	3.5×10^{-3}	$m_1 = 4.8$ $m_2 = 12$	$\sigma_{01} = 5200$ $\sigma_{02} = 6100$	10	3.0	1.11	40	42×10^{-3}	0.5	1.54	55
M40-Epoxy	392.0	155.55	3.0×10^{-3}	16	4500	25	3.5	1.29	50	36×10^{-3}	0.18	25	60
AS4 -Epoxy	234.0	92.85	3.5×10^{-3}	10.7	4275	12.7	3.76	1.39	50	-	-	$15\times R$	60
M50S	480.0	190.48	2.65×10^{-3}	9	4600	10				-	-	$15\times R$	60

Table 2: UD composites and model properties.

Table 3:

Composite	Experimental test	*SCF* model	Variable	RVE width and thickness size (R is the fibre radius)			
				$50\times R$	$100\times R$	$150\times R$	$200\times R$
T700S-Epoxy	1.89 % [18]	Swolfs *et al.*	Failure strain [%]	2.23 ± 0.07	2.18 ± 0.08	2.16 ± 0.07	2.15 ± 0.07
			Failure stress [MPa]	5341 ± 143	5287 ± 121	5264 ± 124	5243 ± 123
			CPU time [h:mm:ss]	0:01:28	0:06:00	0:15:10	0:34:50
		Eitan and Wagner	Failure strain [%]	2.33 ± 0.05	2.22 ± 0.04	2.15 ± 0.03	2.07 ± 0.02
	4740 MPa (*)		Failure stress [MPa]	5491 ± 121	5352 ± 64	5219 ± 62	5075 ± 52
			CPU time [h:mm:ss]	0:03:20	0:28:12	1:49:47	4:37:00
		Zhou and Wagner	Failure strain [%]	2.31 ± 0.06	2.20 ± 0.05	2.13 ± 0.05	2.07 ± 0.04
			Failure stress [MPa]	5486 ± 112	5332 ± 84	5203 ± 104	5081 ± 73
			CPU time [h:mm:ss]	0:03:14	0:25:59	1:40:16	4:59:00
M40-Epoxy	0.976 % (*)	Swolfs *et al.*	Failure strain [%]	1.09 ± 0.03	1.08 ± 0.02	1.07 ± 0.03	1.06 ± 0.03
			Failure stress [MPa]	2584 ± 73	2561 ± 51	2534 ± 66	2511 ± 60
			CPU time [h:mm:ss]	0:02:08	0:13:36	0:45:41	1:09:00
		Eitan and Wagner	Failure strain [%]	1.18 ± 0.03	1.13 ± 0.03	1.11 ± 0.02	1.09 ± 0.01
	2310 MPa [42]		Failure stress [MPa]	2768 ± 52	2657 ± 57	2610 ± 46	2572 ± 31
			CPU time [h:mm:ss]	0:03:42	0:22:43	0:42:28	2:53:00
		Zhou and Wagner	Failure strain [%]	1.14 ± 0.02	1.10 ± 0.02	1.08 ± 0.02	1.07 ± 0.02
			Failure stress [MPa]	2676 ± 50	2589 ± 51	2546 ± 49	2521 ± 54
			CPU time [h:mm:ss]	0:02:51	0:27:26	0:24:22	2:30:00

Table 3: Obtained failure strains and stress with 95% normal distribution confidence intervals for 40 realizations of each RVE size and *SCF* model. T700S failure stress corresponds to the fibre failure stress, whereas M40 corresponds to the composite failure stress. The CPU times are the mean values for each realization (simulation). Simulations were run on an Intel i7-5820K 3.3GHz processor. (*) Estimated values.